

## Understanding shape selectivity effects of hydroisomerization using a reaction equilibrium model

Sharma, Shrinjay; Rigutto, Marcello S.; Zuidema, Erik; Agarwal, Umang; Baur, Richard; Dubbeldam, David; Vlugt, Thijs J.H.

**DOI**

[10.1063/5.0209210](https://doi.org/10.1063/5.0209210)

**Publication date**

2024

**Document Version**

Final published version

**Published in**

Journal of Chemical Physics

**Citation (APA)**

Sharma, S., Rigutto, M. S., Zuidema, E., Agarwal, U., Baur, R., Dubbeldam, D., & Vlugt, T. J. H. (2024). Understanding shape selectivity effects of hydroisomerization using a reaction equilibrium model. *Journal of Chemical Physics*, 160(21), Article 214708. <https://doi.org/10.1063/5.0209210>

**Important note**

To cite this publication, please use the final published version (if applicable). Please check the document version above.

**Copyright**

Other than for strictly personal use, it is not permitted to download, forward or distribute the text or part of it, without the consent of the author(s) and/or copyright holder(s), unless the work is under an open content license such as Creative Commons.

**Takedown policy**

Please contact us and provide details if you believe this document breaches copyrights. We will remove access to the work immediately and investigate your claim.

RESEARCH ARTICLE | JUNE 04 2024

## Understanding shape selectivity effects of hydroisomerization using a reaction equilibrium model

Special Collection: [Monte Carlo methods, 70 years after Metropolis et al. \(1953\)](#)

Shrinjay Sharma ; Marcello S. Rigutto ; Erik Zuidema; Umang Agarwal ; Richard Baur; David Dubbeldam ; Thijs J. H. Vlugt  

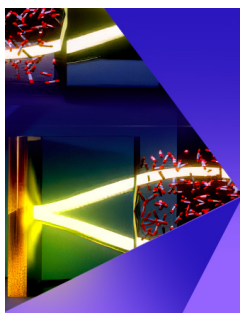
 Check for updates

*J. Chem. Phys.* 160, 214708 (2024)

<https://doi.org/10.1063/5.0209210>



17 June 2024 14:24:29



The Journal of Chemical Physics

Special Topic:  
Polaritonics for Next Generation Materials

Submit Today

 AIP  
Publishing

 AIP  
Publishing

# Understanding shape selectivity effects of hydroisomerization using a reaction equilibrium model

Cite as: J. Chem. Phys. 160, 214708 (2024); doi: 10.1063/5.0209210

Submitted: 19 March 2024 • Accepted: 1 May 2024 •

Published Online: 4 June 2024



View Online



Export Citation



CrossMark

Shrinjay Sharma,<sup>1</sup>  Marcello S. Rigutto,<sup>2</sup>  Erik Zuidema,<sup>2</sup>  Umang Agarwal,<sup>2</sup>  Richard Baur,<sup>2</sup>  David Dubbeldam,<sup>3</sup>  and Thijs J. H. Vlugt<sup>1,a)</sup> 

## AFFILIATIONS

<sup>1</sup> Engineering Thermodynamics, Process and Energy Department, Faculty of Mechanical Engineering, Delft University of Technology, Leeghwaterstraat 39, 2628CB Delft, The Netherlands

<sup>2</sup> Shell Global Solutions International B.V., Amsterdam, The Netherlands

<sup>3</sup> Van 't Hoff Institute of Molecular Sciences, University of Amsterdam, Science Park 904, 1098XH Amsterdam, The Netherlands

**Note:** This paper is part of the JCP Special Topic on Monte Carlo Methods, 70 Years After Metropolis *et al.* (1953).

**a)** Author to whom correspondence should be addressed: [t.j.h.vlugt@tudelft.nl](mailto:t.j.h.vlugt@tudelft.nl)

## ABSTRACT

We study important aspects of shape selectivity effects of zeolites for hydroisomerization of linear alkanes, which produces a myriad of isomers, particularly for long chain hydrocarbons. To investigate the conditions for achieving an optimal yield of branched hydrocarbons, it is important to understand the role of chemical equilibrium in these reversible reactions. We conduct an extensive analysis of shape selectivity effects of different zeolites for the hydroisomerization of C<sub>7</sub> and C<sub>8</sub> isomers at chemical reaction equilibrium conditions. The reaction ensemble Monte Carlo method, coupled with grand-canonical Monte Carlo simulations, is commonly used for computing reaction equilibrium of heterogeneous reactions. The computational demands become prohibitive for a large number of reactions. We used a faster alternative in which reaction equilibrium is obtained by imposing chemical equilibrium in the gas phase and phase equilibrium between the gas phase components and the adsorbed phase counterparts. This effectively mimics the chemical equilibrium distribution in the adsorbed phase. Using Henry's law at infinite dilution and mixture adsorption isotherm models at elevated pressures, we calculate the adsorbed loadings in the zeolites. This study shows that zeolites with cage or channel-like structures exhibit significant differences in selectivity for alkane isomers. We also observe a minimal impact of pressure on the gas-phase equilibrium of these reactions at typical experimental reaction temperatures (400 – 700 K). This study marks initial strides in understanding the reaction product distribution for long-chain alkanes.

© 2024 Author(s). All article content, except where otherwise noted, is licensed under a Creative Commons Attribution-NonCommercial-NoDerivs 4.0 International (CC BY-NC-ND) license (<https://creativecommons.org/licenses/by-nc-nd/4.0/>). <https://doi.org/10.1063/5.0209210>

## I. INTRODUCTION

In transitioning toward fuels and chemicals from renewable sources, platforms that provide clean hydrocarbon liquid energy carriers derived from carbon dioxide directly or via bio-components can play an important role.<sup>1–3</sup> For sustainable aviation fuel and low carbon gas-oil or lubricants, isoalkanes with high degree of branching are the preferred constituents.<sup>4</sup> Hence, zeolite catalyzed shape selective hydroisomerization,<sup>5</sup> often called catalytic dewaxing, will be a key step in the production of such sustainable fuels and

lubricants, similar to its current application in refineries and gas-to-liquid technology.<sup>6,7</sup>

The process of transforming normal alkanes into branched isomers in the presence of H<sub>2</sub> is known as hydroisomerization of alkanes.<sup>8</sup> In hydroisomerization reactions, linear alkanes are adsorbed and dehydrogenated at the metal sites of the zeolites.<sup>9</sup> This leads to the formation of alkenes, which migrate to the acid sites of the zeolites. These alkenes form alkylcarbenium ions via protonation, which are transferred to the metal sites where alkanes are produced through hydrogenation reactions.<sup>9</sup> Hydroisomerization

reactions are generally performed in a special category of nanoporous materials called zeolites.<sup>10</sup> Zeolites are important for selective production and separation of branched hydrocarbons,<sup>11</sup> the ability to sort molecules primarily based on size exclusion.<sup>12</sup> This is due to a regular pore structure of molecular dimensions. The maximum size of the molecular species that can enter the zeolite pores is controlled by the channel dimensions.<sup>12</sup> It is very important to understand the role of the shapes and sizes of channels present in different zeolites for determining the selectivity of the hydroisomerization process.<sup>13</sup> This is because hydroisomerization reactions produce a large number of isomers and cracked products. The number of isomers formed increases rapidly with the increase in the carbon chain length.<sup>14</sup> Therefore, a detailed analysis of the reaction product distribution in experiments is not always possible.

Hydroisomerization reactions are reversible in nature. To identify the conditions that can potentially yield optimal reaction products, it is important to comprehend the role of chemical equilibrium in these reactions. Estrada-Villagrana *et al.*<sup>15</sup> modeled the hydroisomerization of a mixture of alkanes ( $C_6$ ,  $C_7$ ,  $C_8$ , and  $C_9$ ) in Pt/USY (Ultra stable Y)-type zeolites at reaction equilibrium. These authors studied the following cases: (1) hydroisomerization with no restriction to cracking reactions, (2) limiting the cracking of 33m $C_5$  and 223m $C_5$  isomers, and (3) a system without any cracking reaction. The reaction product distribution closest to experimental results<sup>16</sup> was obtained by limiting the cracking of 33m $C_5$  and 223m $C_5$  isomers.<sup>15</sup> The selectivities obtained for the case without any cracking reaction (Case 3) differed significantly from the experimental results, which involved only reaction products due to isomerization. In the experiments,<sup>16</sup> the cracking of longer chain isomers (e.g.,  $C_9$ ) was observed.<sup>15</sup> However, Estrada-Villagrana *et al.*<sup>15</sup> emphasized the importance of analyzing such systems (case 3) at reaction

equilibrium to enhance selectivity toward isomerization over cracking reactions. In addition, comparing reaction equilibrium distribution with data from experiments or kinetic models helps us to distinguish between thermodynamic and kinetic contributions to the reaction product distribution. Steijns *et al.*<sup>17</sup> performed experiments of hydroisomerization of  $C_{10}$  molecules on Pt/Y-type zeolites and compared the results to reaction equilibrium data<sup>18</sup> obtained from the literature. These authors have observed that following the hydroconversion process, the fraction of n- $C_{10}$  in the mixture is larger than the corresponding fraction at equilibrium. The concentrations of the di-branched and multi-branched isomers are always lower than the thermodynamic equilibrium data.<sup>17</sup> Steijns *et al.*<sup>17</sup> have concluded that for a mixture of isomers with the same degree of branching, thermodynamic equilibrium is reached at medium conversion  $\sim(40\% - 70\%)$ . For a mixture of isomers with varying degrees of branching, equilibrium is never reached. This aligns with the widely accepted carbenium ion mechanism.<sup>17</sup> In this work, reaction equilibrium distribution of hydroisomerization of  $C_7$  and  $C_8$  isomers is studied, which will serve as the first step toward understanding the reaction product distribution of hydroisomerization, which is influenced by adsorption of reactants, reaction kinetics, diffusion of molecules inside zeolites, and desorption of reaction products.<sup>5,12</sup> The aim of this study is to understand the shape selectivity effects of FAU-, ITQ-29-, BEA-, MEL-, MFI-, MTW-, and MRE-type zeolites (Fig. 1) on hydroisomerization of  $C_7$  and  $C_8$  isomers at reaction equilibrium. This study does not account for reaction kinetics and diffusion of isomers inside zeolites. Cracking reactions, being irreversible<sup>19</sup> in nature, are also excluded from this analysis. For modeling of cracking reactions, the reader is referred to Ref. 20. Future investigations will aim at understanding the reaction product distributions for the isomerization of long-chain alkanes and to which extent chemical equilibrium is applicable.

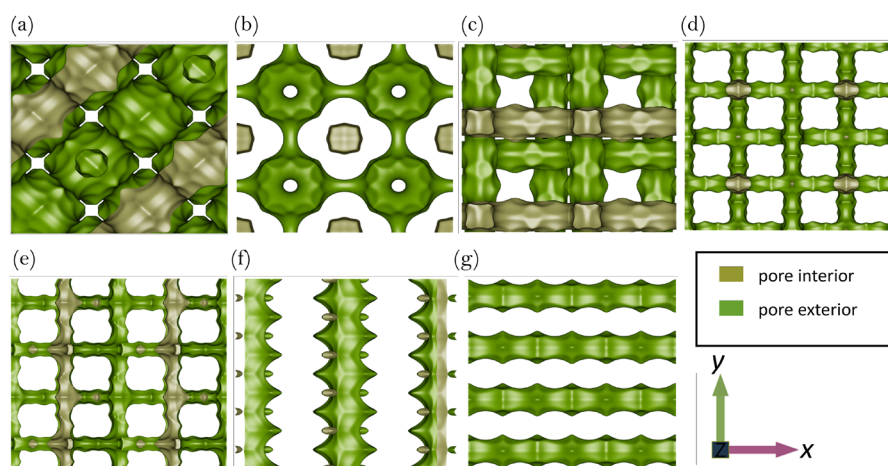


**FIG. 1.** Typical representations of pore structures of (a) FAU-, (b) ITQ-29-, (c) BEA-, (d) MEL-, (e) MFI-, (f) MTW-, and (g) MRE-type zeolites. The FAU-type zeolite has cage-like pore structures. The ITQ-29-type zeolite also has cage-like pore structures connected by narrow channels. The three-dimensional network of straight channel-like pores in both vertical and horizontal directions is present in BEA- and MEL-type zeolites. The MFI-type zeolite has sinusoidal shaped channels in the horizontal direction and straight channels in the vertical direction. MTW- and MRE-type zeolites contain one-dimensional channel-like pores in vertical and horizontal directions, respectively. In these representations, the horizontal direction is represented by the  $x$  axis and vertical direction is represented by the  $y$  axis. The iRASPA software<sup>21</sup> was used to generate these images.

Achieving chemical reaction equilibrium in experiments is a challenging task as hydroisomerization reactions are always accompanied by irreversible cracking reactions. An alternative pathway to study reaction equilibria is by performing Reaction Ensemble Monte Carlo (RxMC) simulations<sup>22–24</sup> using a classical force field-based description of hydrocarbon–zeolite and hydrocarbon–hydrocarbon interactions. Grand-Canonical Monte Carlo (GCMC) simulations coupled with reaction ensemble can be used to compute the chemical equilibrium distribution.<sup>25,26</sup> Another way to compute the adsorbed phase reaction equilibrium distribution is by using the RxMC method in the constant pressure Gibbs ensemble (GENPT).<sup>25,27</sup> The reaction ensemble trial moves involve the removal of randomly selected reactant molecules and insertion of reaction product molecules simultaneously.<sup>24,28</sup> The efficiency of this algorithm is low for systems with high molecule densities and a large number of independent reactions.<sup>24,28</sup> Therefore, these methods can become computationally very time consuming for studying the hydroisomerization of alkanes, which consists of a large number of possible reactions, especially for long-chain hydrocarbons. There is a faster alternative to compute reaction equilibrium distributions when chemical reactions and phase equilibrium occur simultaneously.<sup>15,29</sup> This method has several requirements: (1) Each species should achieve phase equilibrium between all phases. (2) The reactions must be in chemical equilibrium in each phase. For a system at constant temperature and pressure, the Gibbs free energy of the system is minimum<sup>29</sup> at equilibrium. The chemical reaction equilibrium distribution can be obtained by minimizing the molar Gibbs free energy of the system with respect to variations that are consistent with the stoichiometry of the chemical reactions.<sup>29</sup> For mono-molecular reactions, this can be achieved by simply equating the Gibbs free energies or the chemical potentials of the components present in the reaction equilibrium mixture. A detailed explanation of this method is provided in Sec. II of this study. Here, we impose chemical equilibrium in the gas phase for the hydroisomerization of alkanes and phase equilibrium of the isomers between the gas and the adsorbed phase. This automatically mimics the reaction equilibrium conditions in the adsorbed phase. Therefore, the adsorbed phase distribution is the reaction equilibrium distribution in this case. At reaction equilibrium, the chemical equilibrium of alkenes as intermediates may play an important role. In this study, we consider only the reaction equilibrium of the alkane isomers involved in the reactions. This is due to the lack of availability of thermodynamic data for the corresponding alkene intermediates. We consider equilibrium between dehydrogenation of alkanes into alkenes, protonation of alkenes to form alkylcarbenium ions, and formation of corresponding alkane isomers via hydrogenation. The reaction equilibrium distribution at both infinite dilution and high pressures is investigated. The gas phase equilibrium distribution at infinite dilution is computed using the ideal gas chemical potential,<sup>30–32</sup> and the corresponding distribution in the adsorbed phase is calculated using Henry's law.

This article is organized as follows. The important concepts and the theory behind the method to compute reaction equilibrium distributions are discussed in Sec. II. The simulation techniques used in this study are explained in detail in Sec. III. In Sec. IV, the shape selectivity effects of different zeolites on the Henry coefficients and the reaction equilibrium distribution of C<sub>7</sub> isomers at both infinite dilution and finite loading conditions are analyzed. It is observed

that multi-branched isomers are favored in cage-like structures (ITQ-29-type zeolite) and mono-branched isomers are favored in the channel-like structures. At high pressures, the gas phase composition is computed by considering deviations from ideal gas behavior. The adsorbed phase distribution at finite loadings is obtained using Ideal Adsorbed Solution Theory (IAST).<sup>33,34</sup> It is observed that the gas phase equilibrium distribution is not significantly influenced by the gas phase pressure, especially at temperatures equal to or above 500 K. Therefore, variations in the selectivity in the adsorbed phase are influenced by the pure component adsorption isotherm parameters, which are used as input for mixture isotherm calculations. In Sec. V, we discuss conclusions on how the shape selectivity of various zeolites influences the hydroisomerization reaction. This article also contains a [supplementary material](#) (SI1.pdf and SI2.xlsx). The force field parameters required for the calculations of the Henry coefficients are listed in the [supplementary material](#), SI1.pdf. Results and raw data (Henry coefficients and adsorbed phase selectivities) pertaining to C<sub>8</sub> isomers are also included in the file SI1.pdf. The chemical thermodynamic data for C<sub>7</sub> and C<sub>8</sub> isomers obtained from the thermodynamic tables by Scott<sup>35</sup> are listed in the [supplementary material](#), SI2.xlsx. The file SI2.xlsx also contains data for the gas phase distribution of C<sub>7</sub> and C<sub>8</sub> isomers at reaction equilibrium. Additionally, the Henry coefficients, gas phase selectivity, adsorbed phase selectivity data at infinite dilution, the pure component fugacity coefficients, and the gas phase distribution at finite loadings for these isomers are included in SI2.xlsx. The nomenclature for all of these isomers is listed in the worksheet Intro of SI2.xlsx.

## II. THEORY

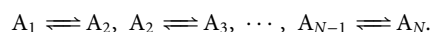
In the context of chemical reaction equilibria, chemical equilibrium is defined by the summation of the product of stoichiometric coefficients and the chemical potentials of each component equating to zero,<sup>36</sup>

$$\sum_{r=1}^{N_r} \nu_r \mu_r + \sum_{p=1}^{N_p} \nu_p \mu_p = 0. \quad (1)$$

Here,  $\nu$  is the stoichiometric coefficient of each component participating in the reaction and  $\mu$  is the chemical potential for each of these components. The subscript  $r$  indicates reactants and  $p$  denotes reaction products. For mono-molecular reactions, this equation can be simplified as the chemical potentials of the reactant and reaction product become equal,

$$\mu_r = \mu_p. \quad (2)$$

This leads to a computationally faster method in calculating reaction equilibrium distribution compared to RxMC simulations. This study primarily concentrates on hydroisomerization reactions, which are mono-molecular in nature. The modeling framework explained here remains valid for other heterogeneous mono-molecular reactions. Consider a system of such reactions involving hydrocarbon chains ( $A_1, A_2, \dots, A_N$ ),



According to Eq. (2), we have

$$\mu_{\text{ads},A_1} = \mu_{\text{ads},A_2} = \mu_{\text{ads},A_3} = \dots = \mu_{\text{ads},A_N}. \quad (3)$$

This scenario is analogous to a fluid mixture undergoing adsorption, where the gas phase composition reaches chemical equilibrium. By enforcing gas phase equilibrium for a mixture comprising of components ( $A_1, A_2, \dots, A_N$ ), we obtain

$$\mu_{\text{gas},A_1} = \mu_{\text{gas},A_2} = \mu_{\text{gas},A_3} = \dots = \mu_{\text{gas},A_N}. \quad (4)$$

At adsorption equilibrium, the chemical potential of the components in the gas phase and the adsorbed phase is equal, so we have

$$\mu_{\text{ads},A_1} = \mu_{\text{gas},A_1}, \quad \mu_{\text{ads},A_2} = \mu_{\text{gas},A_2}, \quad \mu_{\text{ads},A_3} = \mu_{\text{gas},A_3}, \quad \dots, \quad (5)$$

$$\mu_{\text{ads},A_N} = \mu_{\text{gas},A_N}.$$

Combining Eq. (4) with Eq. (5) yields Eq. (3). This is shown schematically in Fig. 2, which shows that the reaction equilibrium distribution in the adsorbed phase can be ascertained by considering a gas-phase composition at chemical equilibrium at specific temperature and pressure, coupled to the corresponding mixture adsorption isotherms of the individual components involved in the reactions.<sup>25,26</sup> In the scenario of infinite dilution, the mixture adsorption isotherms can be replaced with Henry's law.

To determine the gas mixture at chemical equilibrium, the chemical potentials for each of these components present in the mixture is required. At low gas phase pressure, the chemical potentials of the components in the gas phase mixture can be approximated as the ideal chemical potential ( $\mu_{\text{id},i}$ ),<sup>30,37</sup>

$$\mu_{\text{id},i} = RT \ln \left( \frac{\rho_0}{q_{0,i}} \right) + RT \ln \left( \frac{\rho_i}{\rho_0} \right). \quad (6)$$

In Eq. (6),  $\rho_0$  denotes the reference density, which is chosen to be 1 molecule/ $\text{\AA}^3$ .  $q_{0,i}$  is the isolated molecule partition function,<sup>30–32</sup> and  $\rho_i$  is the number density of the component  $i$ .  $R$  is the universal gas constant, and  $T$  is the absolute temperature. The quantity  $q_{0,i}$  can be computed using quantum chemical software, such as Gaussian.<sup>38</sup> The term  $RT \ln(\rho_0/q_{0,i})$  in Eq. (6) is the reference chemical

potential,  $\mu_{\text{ref},i}$ . This quantity can be calculated using thermodynamic tables, such as Scott's tables<sup>35</sup> and the JANAF tables.<sup>39</sup>  $\mu_{\text{ref},i}$  calculated using Scott's tables equals

$$\mu_{\text{ref},i} = [G_{0,i}(T) - H_{0,i}(T_{\text{ref}})] - D_{0,i}. \quad (7)$$

In Scott's tables, the reference temperature  $T_{\text{ref}}$  is 0 K. In Eq. (7),  $G_{0,i}(T)$  denotes the standard Gibbs free energy of component  $i$  at a specified temperature  $T$ .  $H_{0,i}(0 \text{ K})$  represents the standard enthalpy of formation of component ( $i$ ) at 0 K.  $D_{0,i}$  is the atomization energy computed using Scott's table as follows:

$$D_{0,i} = \sum_{j=1}^{N_{\text{atoms},i}} a_j \Delta_f H_{0,j}(0 \text{ K}) - \Delta_f H_{0,i}(0 \text{ K}). \quad (8)$$

In Eq. (8),  $a_j$  is the number of atoms of type  $j$  present in molecule type  $i$ .  $\Delta_f H_{0,i}$  is the enthalpy of formation of  $i$ . For mono-molecular reactions, equating the ideal gas chemical potentials [Eq. (6)] of the components leads to the ratios of the densities of the reactant and the reaction product in each reaction as follows:

$$\frac{\rho_1}{\rho_2} = \frac{q_{0,1}}{q_{0,2}}. \quad (9)$$

The subscripts 1 and 2 in Eq. (9) represent the reactant and reaction product in the reaction. For a system of  $N$  number of reacting components, Eq. (9) can be extended as follows:

$$\frac{\rho_2}{\rho_1} = \frac{q_{0,2}}{q_{0,1}}, \quad \frac{\rho_3}{\rho_1} = \frac{q_{0,3}}{q_{0,1}}, \quad \dots, \quad \frac{\rho_N}{\rho_1} = \frac{q_{0,N}}{q_{0,1}}. \quad (10)$$

The mole fractions in the gas phase  $y_i$  are calculated using the ratios of the gas phase densities,

$$y_i = \frac{\rho_i}{\sum_{n=1}^N \rho_n}. \quad (11)$$

It is important to note that the error propagation of the gas phase distribution due to uncertainties in the ideal gas chemical

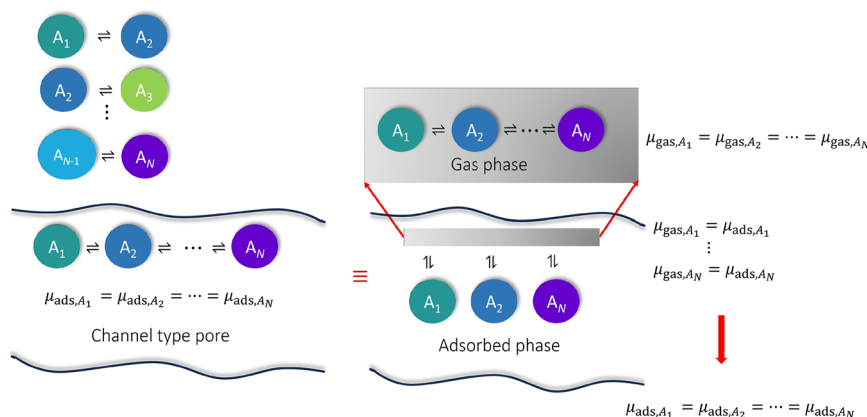


**FIG. 2.** Schematic representation of the modeling framework to compute reaction equilibrium loading in the adsorbed phase. Chemical reaction equilibrium is imposed for the system consisting of  $A_1, A_2, \dots,$  and  $A_N$  type molecules in the gas phase and phase equilibrium between the gas and the adsorbed phase counter-parts. This establishes chemical equilibrium between the molecules in the adsorbed phase.

potentials of C<sub>7</sub> and C<sub>8</sub> isomers is usually negligible. At infinite dilution, the quantity of molecules at reaction equilibrium in the adsorbed phase is determined using Henry's law,

$$q_{\text{load},i} = K_{\text{H},i} P_{\text{tot}} y_i. \quad (12)$$

Here,  $q_{\text{load},i}$  is the amount of adsorbed loading of component  $i$ ,  $K_{\text{H},i}$  is the Henry coefficient of component  $i$ , and  $P_{\text{tot}}$  is the total gas phase pressure of the reacting mixture. The mole fractions in the adsorbed phase  $x_i$  are computed using

$$x_i = \frac{q_{\text{load},i}}{\sum_{n=1}^N q_{\text{load},n}} = \frac{K_{\text{H},i} y_i}{\sum_{n=1}^N K_{\text{H},n} y_n} = \frac{K_{\text{H},i} \rho_i}{\sum_{n=1}^N K_{\text{H},n} \rho_n}. \quad (13)$$

At higher pressures, the chemical potential of a real gas is considered, which is the sum of the ideal gas chemical potential and an excess chemical potential  $\mu_{\text{ex}}$ ,

$$\begin{aligned} \mu_i &= RT \ln \left( \frac{\rho_0}{q_{0,i}} \right) + RT \ln \left( \frac{\rho_i}{\rho_0} \right) + \mu_{\text{ex}} \\ &= RT \ln \left( \frac{\rho_0}{q_{0,i}} \right) + RT \ln \left( \frac{\beta y_i P_{\text{tot}}}{\rho_0} \right) + RT \ln (\phi_i). \end{aligned} \quad (14)$$

In Eq. (14),  $P_{\text{tot}}$  is the total pressure of the mixture.  $\phi_i$  is the fugacity coefficient of component  $i$  in the gas phase. If the total pressure is not too high (typically <10 bars), the fugacity coefficients of the components in a mixture can be estimated using the Lewis and Randall rule,<sup>40</sup>

$$f_i = \phi_{\text{pure},i} y_i P_{\text{tot}}. \quad (15)$$

According to the Lewis and Randall rule, the fugacity  $f_i$  of a component  $i$  in a mixture is equal to the product of the total pressure  $P_{\text{tot}}$ , mole fraction  $y_i$  in the gas phase, and the corresponding pure component fugacity coefficient  $\phi_{\text{pure},i}$  at the same temperature and total pressure. Replacing  $\phi_i$  in Eq. (14) using Eq. (15) leads to

$$\mu_i = RT \ln \left( \frac{\rho_0}{q_{0,i}} \right) + RT \ln \left( \frac{\beta y_i P_{\text{tot}} \phi_{\text{pure},i}}{\rho_0} \right). \quad (16)$$

The ratio of the mole fractions of the reactant and the reaction product in a mono-molecular reaction is computed by combining Eqs. (2) and (16),

$$\frac{y_2}{y_1} = \frac{q_{0,2} \phi_{\text{pure},1}}{q_{0,1} \phi_{\text{pure},2}}. \quad (17)$$

The ratio of the densities of the reaction product and the reactant is equal to the ratio of the corresponding mole fractions,

$$\frac{\rho_2}{\rho_1} = \frac{q_{0,2} \phi_{\text{pure},1}}{q_{0,1} \phi_{\text{pure},2}}. \quad (18)$$

For a system of  $N$  number of reacting components, Eq. (18) can be extended as follows:

$$\begin{aligned} \frac{\rho_2}{\rho_1} &= \frac{q_{0,2} \phi_{\text{pure},1}}{q_{0,1} \phi_{\text{pure},2}}, \quad \frac{\rho_3}{\rho_1} = \frac{q_{0,3} \phi_{\text{pure},1}}{q_{0,1} \phi_{\text{pure},3}}, \quad \dots, \\ \frac{\rho_N}{\rho_1} &= \frac{q_{0,N} \phi_{\text{pure},1}}{q_{0,1} \phi_{\text{pure},N}}. \end{aligned} \quad (19)$$

The ratio of the densities [Eq. (18)] at higher pressure is expressed as the product of the ratio of the densities at infinite dilution [Eq. (9)] and the inverse of the ratio of the fugacity coefficients of the pure components. At higher pressures, the equilibrium loadings are calculated using the Ideal Adsorbed Solution Theory (IAST).<sup>33,34</sup> The mole fractions in the adsorbed phase, denoted by  $x_i$  are calculated using

$$x_i = \frac{q_{\text{load},i}}{\sum_{n=1}^N q_{\text{load},n}}. \quad (20)$$

The selectivity of a component in the gas phase is quantified as<sup>41</sup>

$$s_i^{\text{gas}} = \frac{y_i}{\left( \sum_{n=1}^N y_n \right) - y_i}. \quad (21)$$

To provide insights into the reaction equilibrium distribution in the adsorbed phase, the reaction selectivity is defined as follows:<sup>41</sup>

$$s_i^{\text{ads}} = \frac{x_i}{\left( \sum_{n=1}^N x_n \right) - x_i}. \quad (22)$$

The selectivity of a component in both the gas phase [Eq. (21)] and adsorbed phase [Eq. (22)] is defined as the ratio of the mole fraction of the component to the sum of the mole fractions of all other components present in the same phase,

$$s_{\text{rel},i}^{\text{gas}} = \frac{s_i^{\text{gas}}}{s_{\text{ref}}^{\text{gas}}} = \frac{\frac{y_i}{\left( \sum_{n=1}^N y_n \right) - y_i}}{\frac{y_{\text{ref}}}{\left( \sum_{n=1}^N y_n \right) - y_{\text{ref}}}}, \quad (23)$$

$$s_{\text{rel},i}^{\text{ads}} = \frac{s_i^{\text{ads}}}{s_{\text{ref}}^{\text{ads}}} = \frac{\frac{x_i}{\left( \sum_{n=1}^N x_n \right) - x_i}}{\frac{x_{\text{ref}}}{\left( \sum_{n=1}^N x_n \right) - x_{\text{ref}}}}. \quad (24)$$

To compare selectivity of a component relative to another, the term relative selectivity is defined as the ratio of the absolute selectivity of that component to a reference component as shown in Eqs. (23) and (24) for the gas ( $s_{\text{rel},i}^{\text{gas}}$ ) and the adsorbed phase ( $s_{\text{rel},i}^{\text{ads}}$ ), respectively. In this study, n-C<sub>7</sub> and n-C<sub>8</sub> molecules are chosen as reference components for computing relative selectivities.

### III. SIMULATION DETAILS

To determine the ratios of the densities of the isomers at chemical equilibrium, the reference chemical potential  $\mu_{\text{ref},i}$  [Eq. (7)] is a crucial parameter. To compute this, thermodynamic tables by Scott<sup>35</sup> are used. The detailed raw datasets essential for these calculations, which are obtained from these tables, are available in the [supplementary material](#), SI2.xlsx, for both C<sub>7</sub> and C<sub>8</sub> isomers.

At infinite dilution, the adsorbed loadings are calculated using Henry's law [Eq. (12)]. The equilibrium loading of each isomer is proportional to the corresponding Henry coefficient  $K_{\text{H}}$ . Henry coefficients are computed using the Widom test particle insertion method<sup>42</sup> combined with the Configurational-Bias Monte Carlo (CBMC) method.<sup>43–45</sup> Alkanes are modeled using the united-atom model.<sup>46</sup> This model is found to be accurate while being computationally cost-efficient<sup>47</sup> because the united-atoms (C, CH, CH<sub>2</sub>, and CH<sub>3</sub>) are charge-neutral and the Coulomb interactions can be omitted.<sup>48</sup> The TraPPE united-atom force field<sup>47</sup>

**TABLE I.** Total number of unit cells for different zeolites used in the simulations to compute the Henry coefficients of  $C_7$  and  $C_8$  isomers, along with the dimensions and void fractions of these zeolites.<sup>55</sup>

Zeolite	Number of unit cells	Unit cell dimension (Å)			Void fraction
		<i>a</i>	<i>b</i>	<i>c</i>	
FAU-type	8 (2 × 2 × 2)	24.35	24.35	24.35	0.49
ITQ-29-type	27 (3 × 3 × 3)	11.92	11.92	11.92	0.403
BEA-type	4 (2 × 2 × 1)	12.66	12.66	26.41	0.41
MEL-type	8 (2 × 2 × 2)	20.27	20.27	13.46	0.28
MFI-type	8 (2 × 2 × 2)	20.09	19.74	13.14	0.29
MTW-type	36 (2 × 9 × 2)	25.55	5.26	12.12	0.21
MRE-type	20 (5 × 2 × 2)	8.26	14.56	20.31	0.16

is used for the intramolecular bonded interactions, which include bond-stretching, bond-bending, and torsion interactions. All parameters necessary for intramolecular bonded potentials are listed in Tables S3–S5 of the [supplementary material](#), SI1.pdf. The non-bonded interactions between the adsorbent and the adsorbate as well as the intramolecular non-bonded interactions are modeled using Lennard-Jones interactions.<sup>49</sup> For non-bonded inter-adsorbate interactions, the Lennard-Jones parameters for each component are obtained from the work of Dubbeldam *et al.*,<sup>50</sup> which are listed in Table S1 of the [supplementary material](#), SI1.pdf. The TraPPE-zeo force field<sup>51</sup> is used for the non-bonded interactions between the adsorbate and the adsorbent. All silica zeolites are considered as rigid structures.<sup>52</sup> The influence of zeolite flexibility is negligible on adsorption processes, especially at infinite dilution.<sup>52</sup> The Lennard-Jones parameters for zeolite atoms are listed in Table S2 of the [supplementary material](#), SI1.pdf. Lennard-Jones interactions are truncated and shifted at 12 Å without applying tail corrections. To account for these interactions between different types of atoms, the Lorentz–Berthelot<sup>53,54</sup> mixing rules are used. The force field parameters used in this study are extensively validated and can perfectly reproduce experimental adsorption results.<sup>50,51</sup> **Table I** lists the number of unit cells in the simulation box for each zeolite, along with the respective dimensions and the void fractions of these zeolites. The results for the hydroisomerization of  $C_7$  isomers

in these zeolites are included in Sec. IV, while the results pertaining to  $C_8$  isomers are presented in the [supplementary material](#), SI1.pdf.

To calculate the ratios of the gas phase densities of the isomers at high pressures, the computations require pure component fugacity coefficients corresponding to the total pressure of the mixture [Eq. (19)]. These values are determined using the Peng–Robinson equation of state,<sup>56</sup> which requires the magnitudes of critical temperature, critical pressure, and acentric factors as input. These critical parameters are listed in the worksheet *Critical\_consts* of the [supplementary material](#), SI2.xlsx. The adsorbed phase equilibrium loadings at high pressures are calculated using Ideal Adsorbed Solution Theory (IAST). Pure component adsorbed loadings at various pressures ( $10^1$ – $10^8$  Pa) are computed using the Grand-Canonical Monte Carlo (GCMC) simulations coupled with the CBMC-algorithm using the RASPA software.<sup>48,57</sup> For details on computing adsorption isotherms using GCMC simulations, the reader is referred to Refs. 58 and 59. The pure component adsorbed loadings are fitted to the single site Langmuir-type isotherm equation. The fitted parameters (**Table II**) are used as input in calculating adsorbed phase loadings of mixtures. The effect of higher pressure on the adsorption of  $C_7$  isomers in MTW-type zeolites is studied using the same number of unit cells for the simulation box as specified in **Table I**. The pure component isotherm parameters for different isomers in MTW-type zeolites at 500 K are shown in **Table II**.

**TABLE II.** Pure component Langmuir-type isotherm parameters for adsorption of  $C_7$  isomers in MTW-type zeolites at 500 K obtained by fitting to the results from CBMC simulations in the grand-canonical ensemble.

Isomer	Saturation loading (mol/kg zeolite)	Langmuir constant (1/Pa)
n- $C_7$	0.471	$1.12 \times 10^{-3}$
2m $C_6$	0.476	$4.97 \times 10^{-4}$
3m $C_6$	0.479	$1.99 \times 10^{-4}$
3e $C_5$	0.620	$9.16 \times 10^{-6}$
22m $C_5$	0.496	$4.96 \times 10^{-6}$
23m $C_5$	0.647	$3.09 \times 10^{-5}$
24m $C_5$	0.644	$4.74 \times 10^{-5}$
33m $C_5$	0.504	$2.80 \times 10^{-6}$
223m $C_4$	0.486	$1.20 \times 10^{-6}$

#### IV. RESULTS AND DISCUSSIONS

The considered zeolites exhibit diverse pore shapes and sizes, such as cage-like structures (FAU- and ITQ-type zeolites), channels with intersections (MEL-, MFI-, and BEA-type zeolites), and one-dimensional channel-type zeolites (MRE- and MTW-type zeolites). We extensively analyze shape selectivity effects of the zeolites at infinite dilution for  $C_7$  isomers. Additionally, the effect of pressure on the equilibrium distribution of  $C_7$  isomers inside MTW-type zeolites has been studied. The temperature was varied from 400 to 700 K. The effects of FAU-, ITQ-29-, BEA-, MEL-, MFI-, MTW-, and MRE-type zeolites on hydroisomerization of  $C_7$  isomers are discussed. The shape selectivity effects on hydroisomerization of  $C_8$  isomers are also studied. The results pertaining to  $C_8$  isomers are shown in Figs. S1–S15 of the [supplementary material](#), SI1.pdf. Additionally, the numerical values of the thermochemical properties of all

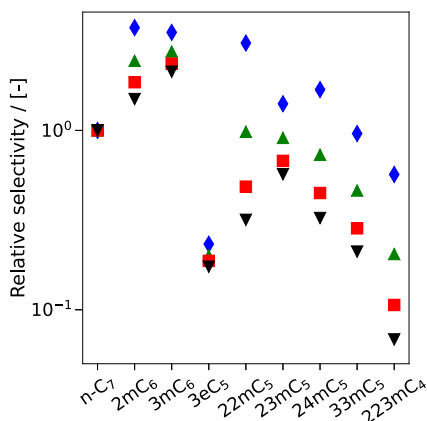


**FIG. 3.** Relative selectivities of different  $C_7$  isomers at reaction equilibrium in the gas phase at infinite dilution. The reaction equilibrium distribution is computed at 400 K (blue filled rhombus), 500 K (green filled triangle), 600 K (red filled square), and 700 K (black filled inverted triangle). The raw data are listed in the worksheet `Inq_iC7` of the [supplementary material](#), `SI2.xlsx`.

isomers ranging from  $C_7$  to  $C_8$  isomers listed by Scott<sup>35</sup> are included in the [supplementary material](#), `SI2.xlsx`.

At infinite dilution, the equilibrium distribution of reactions in the adsorbed phase is governed by the interplay between the gas phase distribution and the Henry coefficients. In [Fig. 3](#), the selectivities of  $C_7$  isomers relative to  $n-C_7$  at gas phase equilibrium are shown for temperatures ranging from 400 to 700 K.  $2mC_6$  and  $3mC_6$  exhibit the highest selectivity for all isomers. There is a temperature-dependent shift favoring the selectivity of  $3mC_6$  over  $2mC_6$  at higher temperatures.  $3eC_5$  displays the smallest selectivity for the mono-branched isomers. At 400 K,  $22mC_5$  has the highest selectivity for di-branched molecules. At elevated temperatures (600 and 700 K),  $23mC_5$  has the largest mole fraction for all di-branched isomers.

The selectivity of  $24mC_5$  decreases relative to  $23mC_5$  with increasing temperatures. For the di-branched isomers,  $33mC_5$  is the least favored molecule.  $223mC_4$  has the smallest selectivity compared to the other isomers.

[Figure 4](#) shows the Henry coefficients for  $C_7$  isomers in FAU- and ITQ-29-type zeolites for a temperature range of 400–700 K. The FAU-type zeolite shows small variations in adsorption selectivity of  $C_7$  isomers. This can be attributed to its large pore diameter (7.4 Å).<sup>55</sup> The geminal alkanes ( $22mC_5$  and  $33mC_5$ ) have the lowest Henry coefficients for di-branched isomers due to the steric hindrance posed by the close proximity of two methyl groups during adsorption. ITQ-29- and FAU-type zeolites show similar affinity for adsorption because of the cage-like pore structures present in these zeolites. [Figure 4\(b\)](#) shows an increase in the Henry coefficients with an increasing degree of branching in the ITQ-29-type zeolite. Such variations are also present in the FAU-type zeolite, but the larger pore size of this zeolite significantly mitigates this effect.  $22mC_5$  and  $33mC_5$  are the least favored di-branched isomers in both ITQ-29- and FAU-type zeolite environments.

BEA-type [[Fig. 5\(a\)](#)] and MEL-type [[Fig. 5\(b\)](#)] zeolites exhibit strikingly similar trends in the variation of Henry coefficients for  $C_7$  isomers. These three-dimensional zeolite structures feature straight channel-type pores with intersections. The channels present in BEA-type zeolites ( $7.6 \times 6.4$  and  $5.5 \times 5.5$ ) Å<sup>2</sup><sup>60</sup> have larger diameters than those in MEL-type zeolites ( $5.3 \times 5.4$ ) Å<sup>2</sup>.<sup>55</sup> An increase in the degree of branching leads to a decrease in Henry coefficients in both zeolites.  $n-C_7$  is the most favored isomer in the channel-type pores of BEA- and MEL-type zeolites.  $3eC_5$ , characterized by the presence of an ethyl group, has the lowest Henry coefficient compared to the other mono-branched isomers.  $22mC_5$ ,  $33mC_5$ , and  $223mC_4$  are the least adsorbed isomers in both zeolites. The proximity of multiple methyl branches in these isomers reduces the preference for adsorption inside the channel-type pores.  $24mC_5$  is the di-branched isomer with the highest affinity for adsorption in both BEA- and MEL-type zeolites. This is attributed to the considerable separation

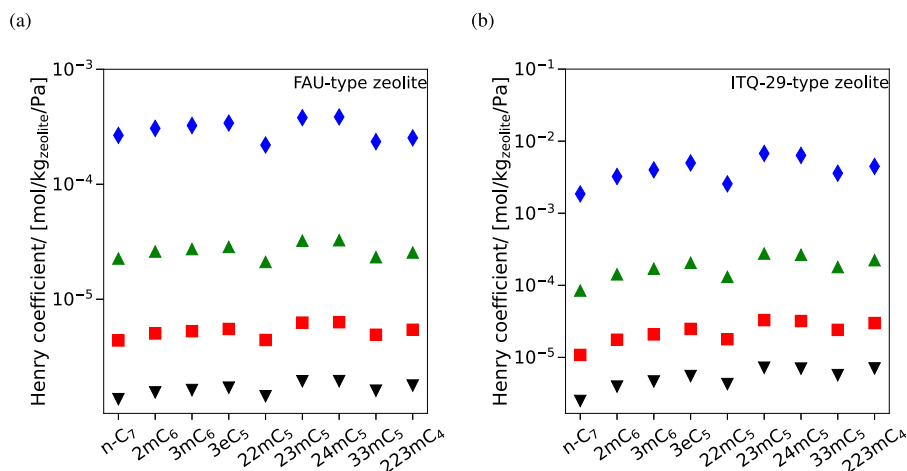


**FIG. 4.** Henry coefficients of  $C_7$  isomers in (a) FAU- and (b) ITQ-29-type zeolites at 400 K (blue filled rhombus), 500 K (green filled triangle), 600 K (red filled square), and 700 K (black filled inverted triangle). The raw data are listed in the worksheets `xi_iC7_400 K`, `xi_iC7_500 K`, `xi_iC7_600 K`, and `xi_iC7_700 K` of the [supplementary material](#), `SI2.xlsx`.

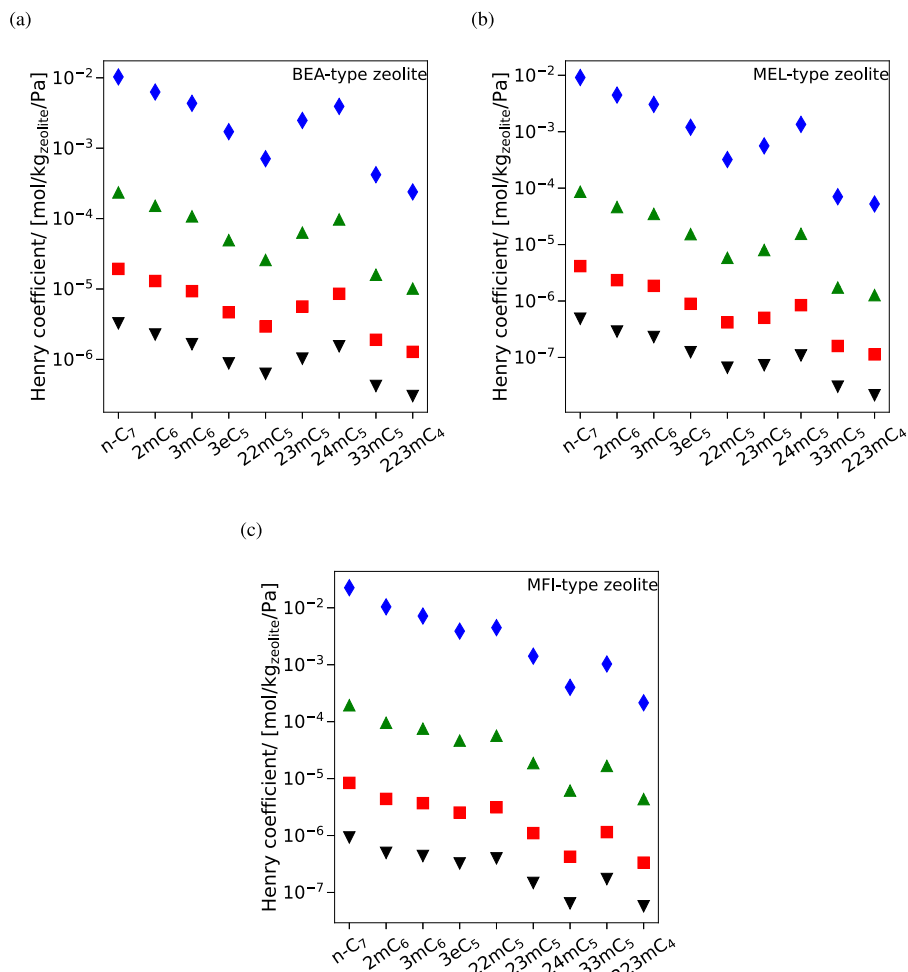


**FIG. 5.** Henry coefficients of  $C_7$  isomers in (a) BEA-, (b) MEL-, and (c) MFI-type zeolites at 400 K (blue filled rhombus), 500 K (green filled triangle), 600 K (red filled square), and 700 K (black filled inverted triangle). The raw data are listed in the worksheets xi\_iC7\_400 K, xi\_iC7\_500 K, xi\_iC7\_600 K, and xi\_iC7\_700 K of the [supplementary material](#), SI2.xlsx.

between the two methyl groups in this particular isomer. In [Fig. 5\(c\)](#), the Henry coefficients for  $C_7$  isomers in MFI-type zeolites are listed. The MFI-type zeolite is also a three-dimensional zeolite structure consisting of channel-like pores connected by intersections.<sup>55</sup> Unlike BEA- and MEL-type zeolites, the MFI-type zeolite is characterized by both sinusoidal and straight channels.<sup>55</sup> Branched isomers preferentially adsorb at channel intersections of MFI-type zeolites,<sup>44,61</sup> while linear alkanes ( $n-C_7$ ) lack such preferences.<sup>44,61</sup> Similar to BEA- and MEL-type zeolites, the MFI-type zeolite also displays decreasing adsorption affinity with an increasing degree of branching. Nevertheless, the preferences for di-branched isomers differ, favoring  $22mC_5$  due to the optimal fit of its two methyl groups at channel intersections [[Fig. 6\(a\)](#)]. As the separation between the methyl groups expands ( $23mC_5$  and  $24mC_5$ ), the probability of either branch attempting to fit into the channel-type pores increases [[Figs. 6\(b\)](#) and [6\(c\)](#)], resulting in an unfavorable scenario. This is because of the smaller diameter of the channels compared to

the intersections.  $33mC_5$  also exhibits preferential adsorption in the MFI-type zeolite, but with a lower Henry coefficient compared to  $22mC_5$ , which can be attributed to the higher steric hindrance experienced by  $33mC_5$ .

[Figures 7\(a\)](#) and [7\(b\)](#) show the Henry coefficients for various  $C_7$  isomers in MTW- and MRE-type zeolites, which feature one-dimensional channel-like pore structures. An overall reduction in the magnitude of Henry coefficients is observed with an increasing degree of branching in both MTW- and MRE-type zeolites. This is consistent with other zeolites with channel-like pore structures (BEA-, MEL-, and MFI-type zeolites). The decrease is sharper than that observed in BEA-, MEL-, and MFI-type zeolites due to smaller pore diameters and the absence of channel intersections. Inside both MTW- and MRE-type zeolites,  $3eC_5$  is the least favored mono-branched isomer. The variations in Henry coefficients in the MTW-type zeolite closely resemble those observed in BEA- and MEL-type zeolites.  $22mC_5$  and  $33mC_5$  are the least preferred di-branched

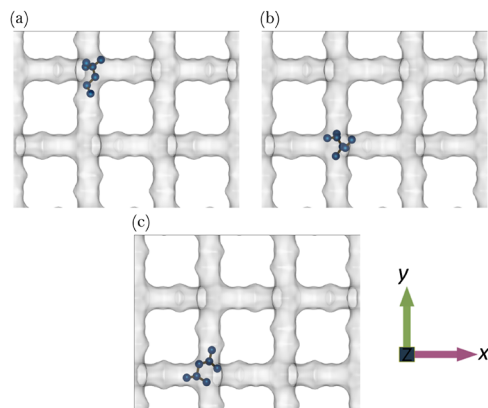


**FIG. 6.** Typical snapshots of adsorption of (a) 22mC<sub>5</sub>, (b) 23mC<sub>5</sub>, and (c) 24mC<sub>5</sub> isomers in MFI-type zeolites at infinite dilution and 500 K. These snapshots are obtained from Monte Carlo simulations of a single molecule inside MFI-type zeolites. In these snapshots, the sinusoidal shaped channels of MFI-type zeolites are located in the horizontal direction and the straight channels are located in the vertical direction. The iRASPA software<sup>21</sup> was used to generate these images.

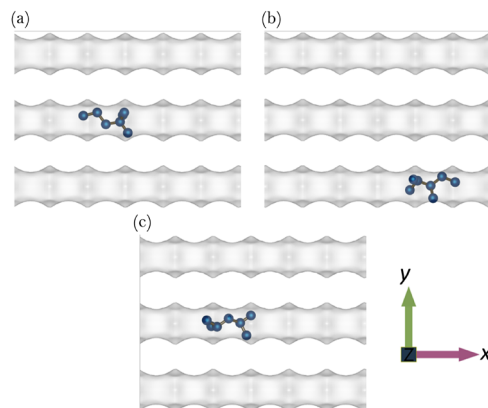


**FIG. 8.** Typical snapshots of adsorption of (a) 22mC<sub>5</sub>, (b) 23mC<sub>5</sub>, and (c) 24mC<sub>5</sub> isomers in MRE-type zeolites at infinite dilution condition and 500 K. These snapshots are obtained from Monte Carlo simulations of a single molecule inside MRE-type zeolites. In these snapshots, one-dimensional channels of MRE-type zeolites are shown in the horizontal direction. The iRASPA software<sup>21</sup> was used to generate these images.

isomers due to steric hindrance posed by the close proximity of the two methyl branches. Similar to the MTW-type zeolite, the MRE-type zeolite also exhibits decreasing Henry coefficients with increasing branching. Larger variations in magnitudes of Henry coefficients can be observed in MRE-type zeolites compared to MTW-type zeolites. Inside the MRE-type zeolite, 23mC<sub>5</sub> is less favored than the 22mC<sub>5</sub> isomer, which is attributed to the corrugations present in the channel-like pores. These corrugations are formed by a combination of peaks and crests, which create regions with varying channel diameters. The higher probability of accommodating both methyl groups in a region with a peak favors the preferential adsorption of 22mC<sub>5</sub>

[Fig. 8(a)] compared to 23mC<sub>5</sub> [Fig. 8(b)] in the MRE-type zeolite. 24mC<sub>5</sub> [Fig. 8(c)] is the most favored di-branched isomer because of the possibility to fit the two methyl branches in the regions where the peaks of the channel corrugations are present.

Adsorption of multi-branched isomers is favored in zeolites with cage-like structures (ITQ-29-type zeolite). Channel-like pore structures, particularly one-dimensional ones without intersections such as in MTW- and MRE-type zeolites, favor the adsorption of linear and mono-branched isomers. The temperature-dependent variations in the Henry coefficients are similar in all zeolites considered in this study. Each isomer shows a reduced affinity for adsorption at

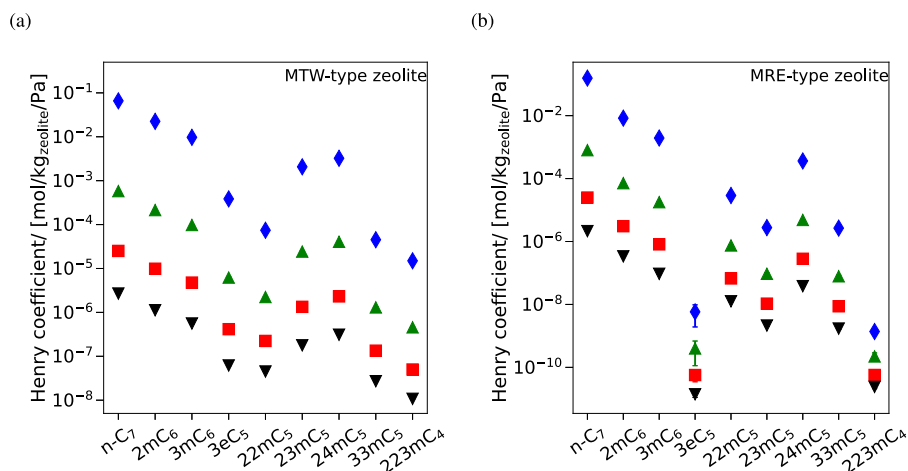


**FIG. 7.** Henry coefficients of C<sub>7</sub> isomers in (a) MTW- and (b) MRE-type zeolites at 400 K (blue filled rhombus), 500 K (green filled triangle), 600 K (red filled square), and 700 K (black filled inverted triangle). The raw data are listed in the worksheets xi\_iC7\_400 K, xi\_iC7\_500 K, xi\_iC7\_600 K, and xi\_iC7\_700 K of the [supplementary material](#), S12.xlsx.

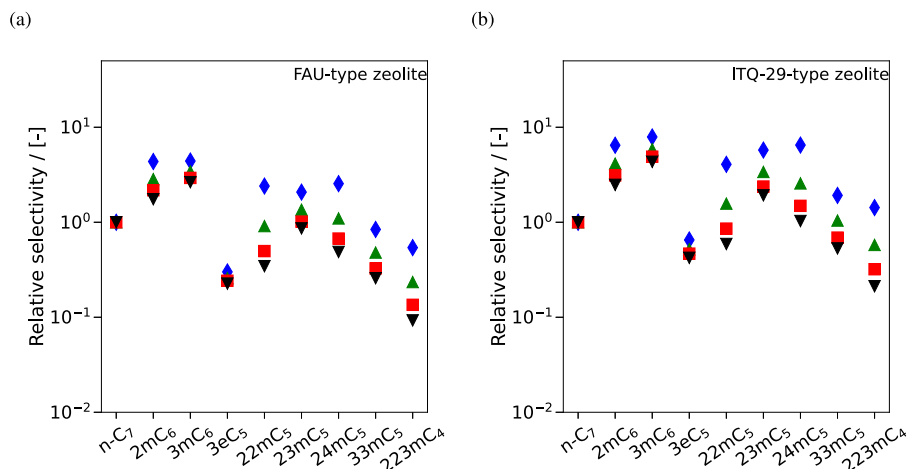


**FIG. 9.** Relative selectivities of different  $C_7$  isomers at reaction equilibrium in (a) FAU- and (b) ITQ-29-type zeolites at infinite dilution. The reaction equilibrium distribution is computed at 400 K (blue filled rhombus), 500 K (green filled triangle), 600 K (red filled square), and 700 K (black filled inverted triangle). The raw data are listed in the worksheets `xi_iC7_400 K`, `xi_iC7_500 K`, `xi_iC7_600 K`, and `xi_iC7_700 K` of the [supplementary material](#), S12.xlsx.

elevated temperatures. Apart from the Henry coefficients, the equilibrium distribution of hydroisomerization reactions in the adsorbed phase is also influenced by the mole fractions of the isomers in the gas phase [Eq. (13)]. At infinite dilution, the gas phase distribution relies solely on the ideal gas reference chemical potential or the isolated molecule partition function [Eq. (6)]. The equilibrium distribution in the adsorbed phase for a system of mono-molecular reactions is determined by the combined influences of the gas phase selectivity and the Henry coefficients. For the FAU-type zeolite, the variations in the adsorbed phase selectivity are similar to those observed in the gas phase selectivity, as shown in Fig. 9(a). This is due to the lack of variation in the magnitudes of the Henry coefficients of  $C_7$  isomers in FAU-type zeolites, irrespective of the degree of branching of these isomers. This is because of the larger pore size in FAU-type zeolites. Similar variations in selectivities can be observed in ITQ-29-type zeolites to certain extent [Fig. 9(b)]. The preference for  $22mC_5$  is consistently lower than that for  $23mC_5$  and  $24mC_5$  in this zeolite, despite  $22mC_5$  being favored over the other two isomers in the gas phase at 400 K. This discrepancy is attributed to the larger influence of the small magnitudes of Henry coefficient compared to the corresponding gas phase selectivity. This is caused by the smaller channel diameters, which connect the cage-type pores in ITQ-29-type zeolites ( $4.1 \text{ \AA}$ )<sup>55</sup> compared to FAU-type zeolites ( $7.4 \text{ \AA}$ ).<sup>55</sup> At temperatures of 500 K and above,  $23mC_5$  exhibits a higher selectivity than  $24mC_5$  in both FAU and ITQ-29-type zeolites. This is favored by both gas phase selectivity and Henry coefficients. ITQ-29- and FAU-type zeolites show lower selectivity for  $223mC_4$  compared to the other isomers. Although  $223mC_4$  preferentially adsorbs in these zeolites, the lower gas phase selectivity plays a dominant role in determining its fraction in the adsorbed phase at reaction equilibrium.

We examine reaction equilibrium distributions of  $C_7$  isomers in zeolites featuring three-dimensional channel-like pore structures.

The selectivities of  $C_7$  isomers relative to  $n-C_7$  in the BEA-type zeolite show an overall decrease with the increasing degree of branching [Fig. 10(a)]. This is influenced by the variations in Henry coefficients of the  $C_7$  isomers in BEA-type zeolites. At 400 K,  $2mC_6$  is favored over  $n-C_7$  and  $3mC_6$ . As temperature increases, the selectivities of  $n-C_7$ ,  $2mC_6$ , and  $3mC_6$  become nearly equal.  $3eC_5$  is the least favored mono-branched isomer due to low gas phase selectivity and a lower Henry coefficient. At low temperatures (500 K and lower),  $24mC_5$  is the most preferred di-branched isomer primarily due to a higher Henry coefficient. At elevated temperatures (600 and 700 K),  $24mC_5$  and  $23mC_5$  exhibit almost identical selectivities.  $33mC_5$  has the lowest selectivity compared to the other di-branched isomers, attributed to the steric hindrances leading to a reduced adsorption affinity. The variations in the selectivities in MEL-type zeolites [Fig. 10(b)] are similar to those in BEA-type zeolites.  $22mC_5$  shows a higher selectivity than  $23mC_5$  at 400 K. At higher temperatures, the difference between the Henry coefficients of these two isomers becomes less significant. The higher selectivity of  $23mC_5$  compared to  $22mC_5$  is mainly caused by the gas phase selectivity. Similar to BEA-type zeolites, the MEL-type zeolite also favors  $24mC_5$  as the most preferred di-branched isomer at lower temperatures (400 and 500 K). At elevated temperatures (700 K),  $24mC_5$  and  $23mC_5$  show nearly identical selectivities because these isomers have Henry coefficients of comparable magnitudes. This is favored by slightly lower gas phase selectivity of  $24mC_5$  compared to  $23mC_5$  at temperatures higher than or equal to 500 K. Selectivities of  $C_7$  isomers relative to  $n-C_7$  in the MFI-type zeolite also show a decreasing trend in the reaction equilibrium distribution with an increasing degree of branching [Fig. 10(c)]. The selectivity of di-branched isomers is highly influenced by Henry coefficients in MFI-type zeolites.  $22mC_5$  is the most favored isomer, and  $24mC_5$  is the least favored isomer. This aligns closely with the Henry coefficients of these two isomers in MFI-type zeolites. The two methyl groups in  $22mC_5$  can

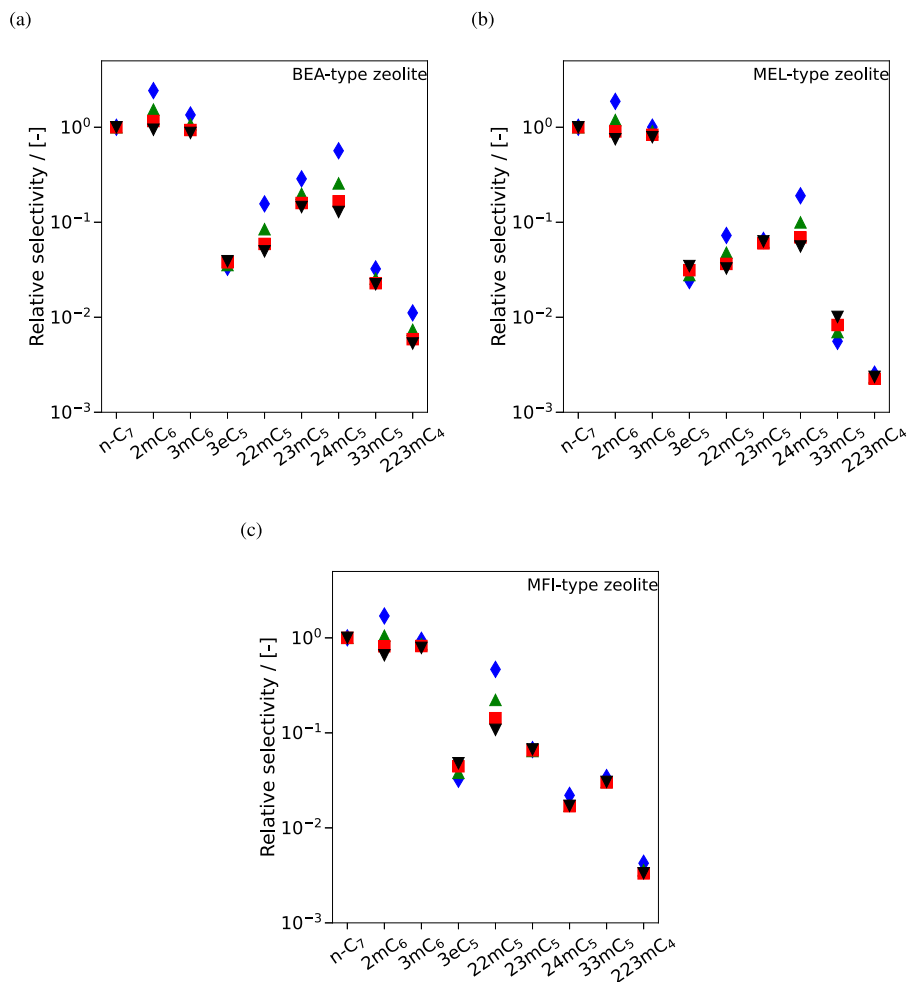


**FIG. 10.** Relative selectivities of different  $C_7$  isomers at reaction equilibrium in (a) BEA-, (b) MEL-, and (c) MFI-type zeolites at infinite dilution. The reaction equilibrium distribution is computed at 400 K (blue filled rhombus), 500 K (green filled triangle), 600 K (red filled square), and 700 K (black filled inverted triangle). The raw data are listed in the worksheets `xi_ic7_400 K`, `xi_ic7_500 K`, `xi_ic7_600 K`, and `xi_ic7_700 K` of the [supplementary material](#), SI2.xlsx.

be optimally accommodated at the intersections of the channel-type pores in MFI-type zeolites. The increasing probability of accommodating one of the methyl groups of  $24mC_5$  inside the channels makes the adsorption of this isomer less favorable than  $22mC_5$ .

Figures 11(a) and 11(b) show the relative selectivities of  $C_7$  isomers in MTW- and MRE-type zeolites. In MTW-type zeolites, the selectivity decreases from  $n-C_7$  to  $3mC_6$  at temperatures larger than or equal to 500 K. The decreasing trend in the Henry coefficients of these isomers plays a dominant role in deciding the corresponding selectivities.  $22mC_5$  has a lower Henry coefficient compared to  $3eC_5$  at all temperatures. The low gas phase selectivity for  $3eC_5$  influences its lower selectivity in the adsorbed phase compared to  $22mC_5$ . Both the Henry coefficient and gas phase selectivity favor  $24mC_5$  compared to other di-branched isomers at 400 K in MTW-type zeolites. The selectivity drops at higher temperatures because

of the decrease in the gas phase selectivity compared to  $23mC_5$ . The relative selectivities in the MRE-type zeolite are similar to the corresponding variations in Henry coefficients. The smaller pore diameters in MRE-type zeolites lead to a larger influence of Henry coefficients compared to the gas phase distribution at chemical equilibrium.

The effects of Henry coefficients on adsorbed phase equilibrium distribution are not prominent in zeolites with larger pore size such as the FAU-type zeolite. While multi-branched isomers are preferably adsorbed in the ITQ-29-type zeolite, such influence on the adsorbed phase reaction equilibrium distribution decreases due to reduced gas phase selectivity. All di-branched isomers exhibit higher selectivities compared to  $n-C_7$  in the ITQ-29-type zeolite. In BEA-, MEL-, and MFI-type zeolites,  $n-C_7$ ,  $2mC_6$ , and  $3mC_6$  have very similar selectivities. Additionally, the mono-branched isomers

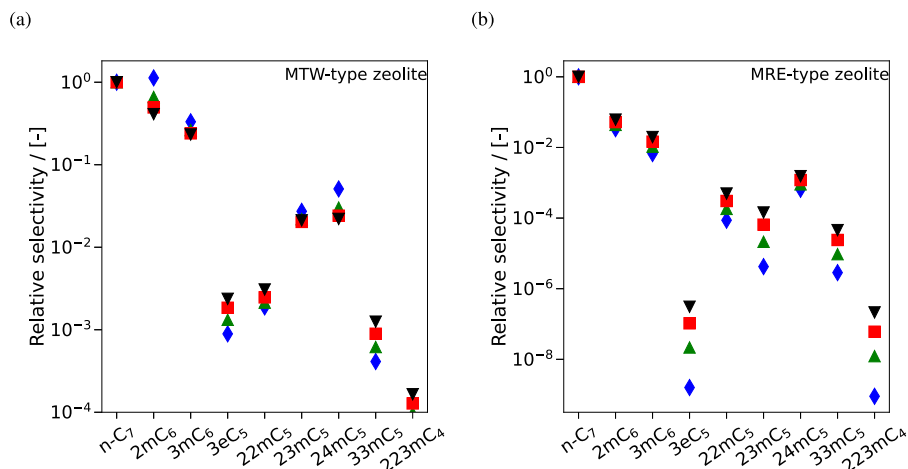


**FIG. 11.** Relative selectivities of different  $C_7$  isomers at reaction equilibrium in (a) MTW- and (b) MRE-type zeolites at infinite dilution. The reaction equilibrium distribution is computed at 400 K (blue filled rhombus), 500 K (green filled triangle), 600 K (red filled square), and 700 K (black filled inverted triangle). The raw data are listed in the worksheets xi\_iC7\_400 K, xi\_iC7\_500 K, xi\_iC7\_600 K, and xi\_iC7\_700 K of the [supplementary material](#), SI2.xlsx.

except for  $3eC_5$  have higher selectivity compared to the di-branched isomers in these zeolites. In zeolites with narrow channel-like pores, such as MRE- and MTW-type zeolites, the affinity of  $C_7$  isomers for adsorption plays an important role in determining adsorbed phase selectivity at reaction equilibrium. MTW- and MRE-type zeolites favor linear isomers ( $n-C_7$ ) the most.  $223mC_4$  is the least favored isomer in all zeolites considered in this study. In this study, it is

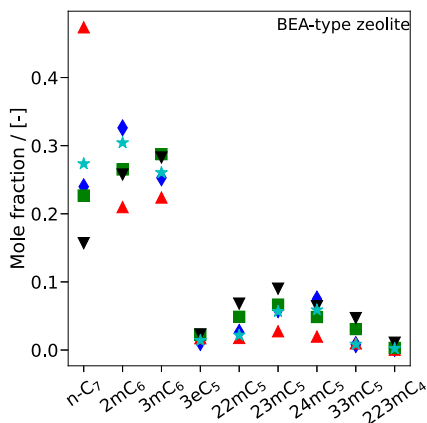


**FIG. 12.** Analysis of reaction product distribution of  $C_7$  isomers in the BEA-type zeolite obtained from experiments by Agarwal *et al.*<sup>19</sup> (red filled triangle, 543.95 K; green filled square, 556.48 K; and black filled inverted triangle, 569.02 K) and computed at chemical equilibrium in this work (blue filled rhombus, 500 K, and blue filled star, 600 K). Cracking reactions are not included in computing reaction equilibrium distribution because of the irreversible nature of these reactions. The mole fractions of the reaction products at temperatures (red filled triangle, 543.95 K; green filled square, 556.48 K; and black filled inverted triangle, 569.02 K) are also calculated without including the cracked products for comparing with the reaction equilibrium distributions (blue filled rhombus, 500 K, and blue filled star, 600 K).

observed that the variations in selectivities between the linear and the branched isomers are significantly influenced by the pore diameter of the zeolite. The channel distributions and the shape of the channels play an important role in determining the differences in the selectivities of isomers with similar degree of branching.

The equilibrium distribution of  $C_7$  isomers in BEA-type zeolites is compared to the results from experiments conducted by Agarwal *et al.*<sup>19</sup> (Fig. 12). These authors have shown a complete reaction network of hydroisomerization of  $C_7$  isomers and possible hydrocracking reactions. It is important to note that the computation of reaction product distribution at chemical equilibrium does not include any cracked products. This is because of the irreversible nature of the cracking reactions. At temperatures smaller than 500 K, negligible conversion of  $n-C_7$  takes place ( $\sim 3\%$ ).<sup>19</sup> There is very high conversion at temperatures above 581.55 K, and the reaction product distribution is mainly composed of cracked products ( $2mC_3$  and  $C_3$  molecules).<sup>19</sup> At intermediate temperatures in the range 543.95–569.02 K, the reaction product distribution is comparable to the molar composition at reaction equilibrium computed in this study (Fig. 12). The distribution obtained from experiments at 556.48 K is closest to the equilibrium distribution. This indicates that at medium conversion (543.95–569.02 K), thermodynamic equilibrium is approached for isomers with similar degree of branching.<sup>17</sup>

Figure 13 shows the distribution of gas phase reaction equilibrium for the hydroisomerization of  $C_7$  isomers at finite loadings. The gas phase distribution remains relatively constant with increasing pressure. Specifically, at 400 K, deviations from infinite dilution conditions are observed at  $\sim 3$  bars, which is due to phase transition. As temperature increases, these deviations become less pronounced. At 500 K, the gas phase distribution deviates from ideal gas behavior at  $\sim 10$  bars, but at higher temperatures (600 and 700 K), these discrepancies become nearly negligible [Figs. 13(c) and 13(d)]. Apart from the reference chemical potential [Eq. (6)], the gas phase distribution

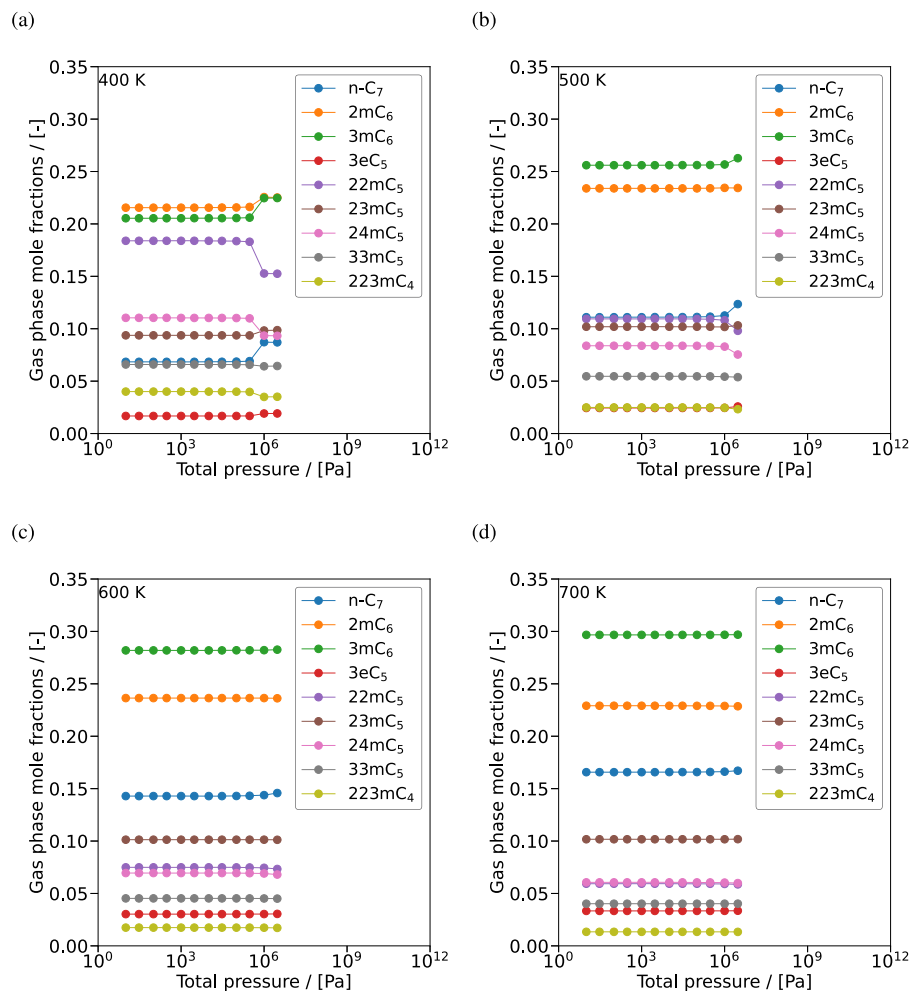


**FIG. 13.** Effect of gas phase pressure on the equilibrium distribution of  $C_7$  isomers at temperatures (a) 400 K, (b) 500 K, (c) 600 K, and (d) 700 K. The raw data are listed in the worksheet InQ\_ic7\_high\_press of the [supplementary material](#), SI2.xlsx.

also depends on the ratios of the corresponding fugacity coefficients. The pure component fugacity coefficients of  $C_7$  isomers at temperatures ranging from 400 to 500 K and pressures ranging from  $1 \times 10^1$  to  $3 \times 10^6$  Pa are listed in the worksheet Fugacity\_ic7 of the [supplementary material](#), SI2.xlsx. There are negligible variations in fugacity coefficients of  $C_7$  isomers at temperatures (500 K or above). Therefore, the fugacity ratios remain close to unity. This leads to negligible deviations in the gas phase distribution with variations in pressure.

The adsorbed phase equilibrium distribution is influenced by the adsorption affinity of the isomers toward the adsorbate. Quantitatively, this can be understood from the pure component adsorption isotherm parameters, which are used as input for computing mixture adsorption isotherms. [Figure 14\(a\)](#) shows the pure

component adsorption isotherms of  $C_7$  isomers in the MTW-type zeolite at 500 K. The isomers with a longer main chain (e.g.,  $n-C_7$ ) are preferred at low pressures. At high pressures, the shorter chains are preferred because of the lack of available space for adsorption. This phenomenon is known as size entropy.<sup>62–64</sup> Mixture adsorption isotherms for  $C_7$  isomers in the MTW-type zeolite at 500 K are shown in [Fig. 14\(b\)](#). The corresponding gas phase composition is considered to be in chemical equilibrium at 500 K. These mixture isotherms are equivalent to the adsorbed phase distribution. The corresponding selectivities of the  $C_7$  isomers relative are illustrated in [Fig. 14\(c\)](#). The absolute selectivities of  $n-C_7$ ,  $2mC_6$ , and  $3mC_6$  decrease with the increasing pressure, whereas the selectivities of the multi-branched isomers increase with the increase in the pressure. This is again due to size entropy effects.<sup>62–64</sup>

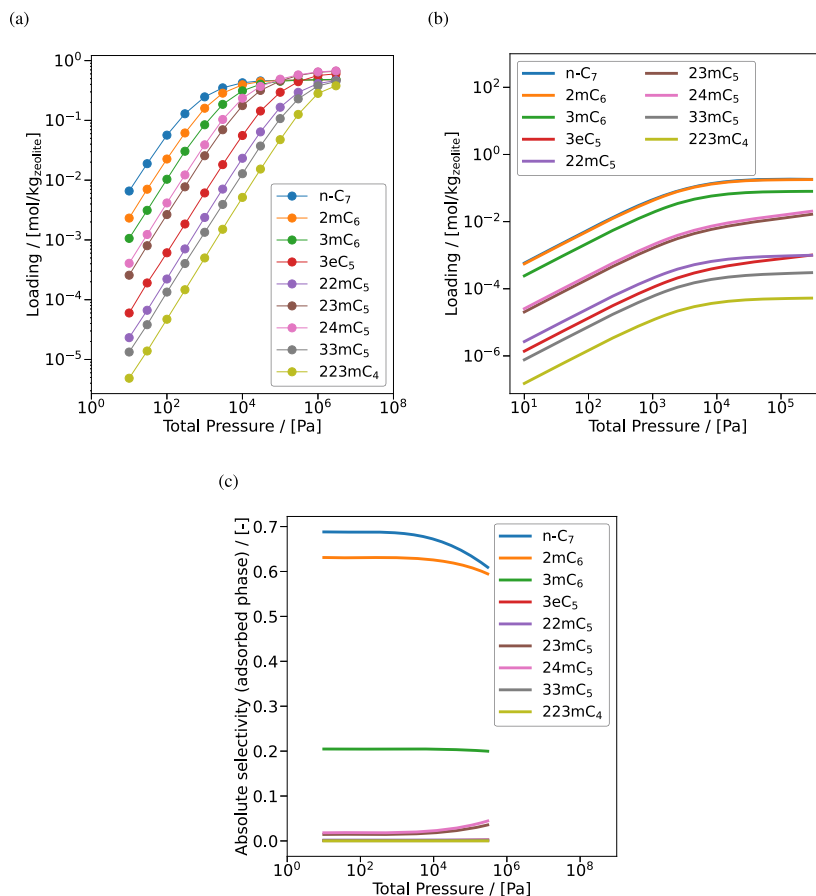


**FIG. 14.** (a) Pure component adsorption isotherms, (b) mixture adsorption isotherms computed using IAST, and (c) reaction equilibrium distribution (absolute selectivities) in the adsorbed phase of C<sub>7</sub> isomers in the MTW-type zeolite at 500 K. The pure component isotherms are fitted to single-site Langmuir-type isotherms.

## V. CONCLUSIONS

Shape selectivity effects of zeolites on C<sub>7</sub> and C<sub>8</sub> isomerization are addressed using a reaction equilibrium model. The equilibrium distribution in the gas phase relies on the isolated molecule partition functions. These are computed using the thermodynamic tables by Scott.<sup>35</sup> The selectivity in the adsorbed phase is determined by the combined effects of the gas-phase distribution and the Henry coefficients. In zeolites with larger pore sizes (FAU-type zeolite), Henry coefficients have a small impact on the adsorbed phase distribution at reaction equilibrium. Multi-branched isomers are favored in zeolites with cage-like structures (ITQ-29-type zeolite). Di-branched isomers consistently have higher selectivity than n-C<sub>7</sub> in ITQ-29-type zeolites. BEA-, MEL-, and MFI-type zeolites exhibit similar selectivities for n-C<sub>7</sub>, 2mC<sub>6</sub>, and 3mC<sub>6</sub>, with a general preference for mono-branched isomers over di-branched isomers. In zeolites with narrow one-dimensional channel-like pores (MRE- and MTW-type zeolites), variations in Henry coefficients play a crucial role in

deciding adsorbed phase reaction equilibrium distribution. MTW- and MRE-type zeolites favor n-C<sub>7</sub> the most. 223mC<sub>4</sub> is the least favored isomer in all zeolites considered in this study. This is due to the presence of multiple methyl branches in close proximity in this isomer, causing steric hindrance. To accommodate the influence of pressure, the consideration of non-ideal gas behavior becomes necessary. The gas-phase distribution is influenced by the ratios of the isolated molecule partition function and the inverse of the ratios of the fugacity coefficients of the components. Increasing pressure hardly affects the gas phase distribution of C<sub>7</sub> isomers at higher temperatures (500–700 K). This is because the values of the fugacity coefficients of the isomers are relatively similar. The selectivities at high pressures are primarily governed by the parameters of the pure component isotherms, which serve as inputs for the mixture isotherm model (IAST). This work will be further continued toward comprehending the reaction product distribution for long-chain alkanes and to which extent chemical reaction equilibrium is reached inside the zeolite.

## SUPPLEMENTARY MATERIAL

This article contains a [supplementary material](#) (SI1.pdf and SI2.xlsx). The force field parameters required for the calculations of the Henry coefficients are listed in the [supplementary material](#), SI1.pdf. Results and raw data (Henry coefficients and adsorbed phase selectivities) pertaining to C<sub>8</sub> isomers are also included in the file SI1.pdf. The chemical thermodynamic and the reaction equilibrium distribution data of C<sub>7</sub> and C<sub>8</sub> isomers are listed in the [supplementary material](#), SI2.xlsx.

## ACKNOWLEDGMENTS

This work was sponsored by NWO Domain Science for the use of supercomputer facilities. This work is part of the Advanced Research Center for Chemical Building Blocks, ARC-CBBC, which is co-funded and co-financed by the Netherlands Organization for Scientific Research (NWO) and the Netherlands Ministry of Economic Affairs and Climate Policy.

## AUTHOR DECLARATIONS

## Conflict of Interest

The authors have no conflicts to disclose.

## Author Contributions

**Shrinjay Sharma:** Investigation (equal); Methodology (equal); Software (equal); Writing – original draft (equal); Writing – review & editing (equal). **Marcello S. Rigutto:** Conceptualization (equal); Funding acquisition (equal); Investigation (equal); Methodology (equal); Software (equal); Supervision (equal); Visualization (equal); Writing – review & editing (equal). **Erik Zuidema:** Conceptualization (equal); Methodology (equal); Project administration (equal); Supervision (equal); Writing – review & editing (equal). **Umang Agarwal:** Funding acquisition (equal); Investigation (equal); Methodology (equal); Supervision (equal); Writing – review & editing (equal). **Richard Baur:** Investigation (equal); Methodology (equal); Writing – review & editing (equal). **David Dubbeldam:** Conceptualization (equal); Funding acquisition (equal); Investigation (equal); Methodology (equal); Software (equal); Supervision (equal); Visualization (equal); Writing – review & editing (equal). **Thijs J. H. Vlugt:** Conceptualization (equal); Funding acquisition (equal); Investigation (equal); Methodology (equal); Project administration (equal); Supervision (equal); Writing – review & editing (equal).

## DATA AVAILABILITY

The data that support the findings of this study are available within the article and its [supplementary material](#).

## REFERENCES

<sup>1</sup>S. van Bavel, S. Verma, E. Negro, and M. Bracht, “Integrating CO<sub>2</sub> electrolysis into the gas-to-liquids–power-to-liquids process,” *ACS Energy Lett.* **5**, 2597–2601 (2020).

<sup>2</sup>V. Kumaravel, J. Bartlett, and S. C. Pillai, “Photoelectrochemical conversion of carbon dioxide (CO<sub>2</sub>) into fuels and value-added products,” *ACS Energy Lett.* **5**, 486–519 (2020).

<sup>3</sup>H. W. Ryu, D. H. Kim, J. Jae, S. S. Lam, E. D. Park, and Y.-K. Park, “Recent advances in catalytic co-pyrolysis of biomass and plastic waste for the production of petroleum-like hydrocarbons,” *Bioresour. Technol.* **310**, 123473 (2020).

<sup>4</sup>H. Calis, W. Lüke, I. Drescher, and A. Schütze, “Synthetic diesel fuels,” in *Handbook of Fuels: Energy Sources for Transportation* (John Wiley & Sons Inc., 2021), pp. 161–200.

<sup>5</sup>B. Smit and T. L. Maesen, “Towards a molecular understanding of shape selectivity,” *Nature* **451**, 671–678 (2008).

<sup>6</sup>M. S. Rigutto, R. van Veen, and L. Huve, “Zeolites in hydrocarbon processing,” *Stud. Surf. Sci. Catal.* **168**, 855–913 (2007).

<sup>7</sup>P. Mäki-Arvela, T. A. Kaka khel, M. Azkaar, S. Engblom, and D. Y. Murzin, “Catalytic hydroisomerization of long-chain hydrocarbons for the production of fuels,” *Catalysts* **8**, 534 (2018).

<sup>8</sup>M. L. Gunawan, T. H. Novita, F. Aprialdi, D. Aulia, A. S. F. Nanda, C. B. Rasrendra, Z. Addarajah, D. Mujahidin, and G. T. M. Kadja, “Palm-oil transformation into green and clean biofuels: Recent advances in the zeolite-based catalytic technologies,” *Bioresour. Technol. Rep.* **23**, 101546 (2023).

<sup>9</sup>A. Poursaeidesfahani, M. F. de Lange, F. Khodadadian, D. Dubbeldam, M. Rigutto, N. Nair, and T. J. H. Vlugt, “Product shape selectivity of MFI-type, MEL-type, and BEA-type zeolites in the catalytic hydroconversion of heptane,” *J. Catal.* **353**, 54–62 (2017).

<sup>10</sup>N. Viswanadham, R. Kamble, S. K. Saxena, and M. Garg, “Studies on octane boosting of industrial feedstocks on Pt/H-BEA zeolite,” *Fuel* **87**, 2394–2400 (2008).

<sup>11</sup>A. Soualah, J. L. Lemberton, L. Pinard, M. Chater, P. Magnoux, and K. Moljord, “Hydroisomerization of long-chain *n*-alkanes on bifunctional Pt/zeolite catalysts: Effect of the zeolite structure on the product selectivity and on the reaction mechanism,” *Appl. Catal., A* **336**, 23–28 (2008).

<sup>12</sup>B. Smit and T. L. M. Maesen, “Molecular simulations of zeolites: Adsorption, diffusion, and shape selectivity,” *Chem. Rev.* **108**, 4125–4184 (2008).

<sup>13</sup>A. Poursaeidesfahani, “Zeolite-based separation and production of branched hydrocarbons,” Ph.D. thesis, Delft University of Technology, 2019.

<sup>14</sup>M. Schenk, “Shape selectivity in zeolites,” Ph.D. thesis, University of Amsterdam, 2003, <https://hdl.handle.net/11245/1.212114>.

<sup>15</sup>A. D. Estrada-Villagrana and C. De La Paz-Zavala, “Application of chemical equilibrium for hydrocarbon isomerization analysis,” *Fuel* **86**, 1325–1330 (2007).

<sup>16</sup>J. F. Denayer, G. V. Baron, G. Vanbutsele, P. A. Jacobs, and J. A. Martens, “Evidence for alkylcarbenium ion reaction intermediates from intrinsic reaction kinetics of C<sub>6</sub>–C<sub>9</sub>*n*-alkane hydroisomerization and hydrocracking on Pt/H–Y and Pt/USY zeolites,” *J. Catal.* **190**, 469–473 (2000).

<sup>17</sup>M. Steijns, G. Froment, P. Jacobs, J. Uytterhaeven, and J. Weitkamp, “Hydroisomerization and hydrocracking. 2. Product distributions from *n*-decane and *n*-dodecane,” *Ind. Eng. Chem. Prod. Res. Dev.* **20**, 654–660 (1981).

<sup>18</sup>D. R. Stull, E. F. Westrum, and G. C. Sinke, *The Chemical Thermodynamics of Organic Compounds*, 1st ed. (John Wiley & Sons, Inc., New York, 1969).

<sup>19</sup>U. Agarwal, M. S. Rigutto, E. Zuidema, A. P. J. Jansen, A. Poursaeidesfahani, S. Sharma, D. Dubbeldam, and T. J. H. Vlugt, “Kinetics of zeolite-catalyzed heptane hydroisomerization and hydrocracking with cbmc-modeled adsorption terms: Zeolite beta as a large pore base case,” *J. Catal.* **415**, 37–50 (2022).

<sup>20</sup>M. D. Macedonia and E. J. Maginn, “Impact of confinement on zeolite cracking selectivity via Monte Carlo integration,” *AIChE J.* **46**, 2504–2517 (2000).

<sup>21</sup>D. Dubbeldam, S. Calero, and T. J. H. Vlugt, “iRASP: GPU-accelerated visualization software for materials scientists,” *Mol. Simul.* **44**, 653–676 (2018).

<sup>22</sup>W. R. Smith and B. Triska, “The reaction ensemble method for the computer simulation of chemical and phase equilibria. I. Theory and basic examples,” *J. Chem. Phys.* **100**, 3019–3027 (1994).

<sup>23</sup>J. K. Johnson, A. Z. Panagiotopoulos, and K. E. Gubbins, “Reactive canonical Monte Carlo: A new simulation technique for reacting or associating fluids,” *Mol. Phys.* **81**, 717–733 (1994).

<sup>24</sup>A. Poursaeidesfahani, R. Hens, A. Rahbari, M. Ramdin, D. Dubbeldam, and T. J. H. Vlugt, “Efficient application of continuous fractional component Monte Carlo in the reaction ensemble,” *J. Chem. Theory Comput.* **13**, 4452–4466 (2017).

- <sup>25</sup>I. Matito-Martos, A. Rahbari, A. Martin-Calvo, D. Dubbeldam, T. J. H. Vlugt, and S. Calero, "Adsorption equilibrium of nitrogen dioxide in porous materials," *Phys. Chem. Chem. Phys.* **20**, 4189–4199 (2018).
- <sup>26</sup>D. O. Wasik, A. Martín-Calvo, J. J. Gutiérrez-Sevillano, D. Dubbeldam, T. J. H. Vlugt, and S. Calero, "Enhancement of formic acid production from carbon dioxide hydrogenation using metal-organic frameworks: Monte Carlo simulation study," *Chem. Eng. J.* **467**, 143432 (2023).
- <sup>27</sup>N. Hansen, S. Jakobtorweihen, and F. J. Keil, "Reactive Monte Carlo and grand-canonical Monte Carlo simulations of the propene metathesis reaction system," *J. Chem. Phys.* **122**, 164705 (2005).
- <sup>28</sup>R. Hens, "Molecular simulation of phase and reaction equilibria: Software and algorithm development," Ph.D. thesis, Delft University of Technology, 2020.
- <sup>29</sup>S. I. Sandler, *Chemical, Biochemical, and Engineering Thermodynamics*, 4th ed. (John Wiley & Sons, NJ, 2017).
- <sup>30</sup>R. Hens, A. Rahbari, S. Caro-Ortiz, N. Dawass, M. Erdős, A. Poursaeidisfahani, H. S. Salehi, A. T. Celebi, M. Ramdin, O. A. Moulto, D. Dubbeldam, and T. J. H. Vlugt, "Brick-CFCMC: Open source software for Monte Carlo simulations of phase and reaction equilibria using the continuous fractional component method," *J. Chem. Inf. Model.* **60**, 2678–2682 (2020).
- <sup>31</sup>H. M. Polat, H. S. Salehi, R. Hens, D. O. Wasik, A. Rahbari, F. De Meyer, C. Houriez, C. Coquelet, S. Calero, D. Dubbeldam, O. A. Moulto, and T. J. H. Vlugt, "New features of the open source Monte Carlo software brick-CFCMC: Thermodynamic integration and hybrid trial moves," *J. Chem. Inf. Model.* **61**, 3752–3757 (2021).
- <sup>32</sup>A. Rahbari, R. Hens, M. Ramdin, O. A. Moulto, D. Dubbeldam, and T. J. H. Vlugt, "Recent advances in the continuous fractional component Monte Carlo methodology," *Mol. Simul.* **47**, 804–823 (2021).
- <sup>33</sup>A. L. Myers and J. M. Prausnitz, "Thermodynamics of mixed-gas adsorption," *AIChE J.* **11**, 121–127 (1965).
- <sup>34</sup>C. Simon, B. Smit, and M. Haranczyk, "pyIAST: Ideal adsorbed solution theory (IAST) Python package," *Comput. Phys. Commun.* **200**, 364–380 (2016).
- <sup>35</sup>D. W. Scott, in *Chemical Thermodynamic Properties of Hydrocarbons and Related Substances: Properties of the Alkane Hydrocarbons, C<sub>1</sub> through C<sub>10</sub>, in the Ideal Gas State from 0 to 1500 K*, 1st ed. (U.S. Department of the Interior, Bureau of Mines, Washington, DC, 1974).
- <sup>36</sup>W. R. Smith and R. W. Missen, *Chemical Reaction Equilibrium Analysis: Theory and Algorithms*, 1st ed. (Wiley, New York, 1982).
- <sup>37</sup>H. M. Polat, F. de Meyer, C. Houriez, O. A. Moulto, and T. J. H. Vlugt, "Solving chemical adsorption equilibria using free energy and quantum chemistry calculations: Methodology, limitations, and new open-source software," *J. Chem. Theory Comput.* **19**, 2616–2629 (2023).
- <sup>38</sup>M. J. Frisch, G. W. Trucks, H. B. Schlegel, G. E. Scuseria, M. A. Robb, J. R. Cheeseman, G. Scalmani, V. Barone, B. Mennucci, G. A. Petersson, H. Nakatsuji, M. Caricato, X. Li, H. P. Hratchian, A. F. Izmaylov, J. Bloino, G. Zheng, J. L. Sonnenberg, M. Hada, M. Ehara, K. Toyota, R. Fukuda, J. Hasegawa, M. Ishida, T. Nakajima, Y. Honda, O. Kitao, H. Nakai, T. Vreven, J. J. Montgomery, J. E. Peralta, F. Ogliaro, M. Bearpark, J. J. Heyd, E. Brothers, K. N. Kudin, V. N. Staroverov, R. Kobayashi, J. Normand, K. Raghavachari, A. Rendell, J. C. Burant, S. S. Iyengar, J. Tomasi, M. Cossi, N. Rega, J. M. Millam, M. Klene, J. E. Knox, J. B. Cross, V. Bakken, C. Adamo, J. Jaramillo, R. Gomperts, R. E. Stratmann, O. Yazyev, A. J. Austin, R. Cammi, C. Pomelli, J. W. Ochterski, R. L. Martin, K. Morokuma, V. G. Zakrzewski, G. A. Voth, P. Salvador, J. J. Dannenberg, S. Dapprich, A. D. Daniels, O. Farkas, J. B. Foresman, J. V. Ortiz, J. Cioslowski, and D. J. Fox, *Gaussian 09, Revision D.01*, Gaussian, Inc., Wallingford, CT, 2009.
- <sup>39</sup>M. W. Chase, *NIST-JANAF Thermochemical Tables*, 4th ed. (American Chemical Society, Washington, DC, 1998), Vol. 9, <https://janaf.nist.gov/>.
- <sup>40</sup>J. B. Ott and J. Boerio-Goates, *Chemical Thermodynamics: Advanced Applications*, 1st ed. (Academic Press, Cornwall, 2000), Vol. 2.
- <sup>41</sup>O. Levenspiel, *Chemical Reaction Engineering*, 3rd ed. (John Wiley & Sons, New York, 1998).
- <sup>42</sup>B. Widom, "Some topics in the theory of fluids," *J. Chem. Phys.* **39**, 2808–2812 (1963).
- <sup>43</sup>T. J. H. Vlugt, M. Martin, B. Smit, J. Siepmann, and R. Krishna, "Improving the efficiency of the configurational-bias Monte Carlo algorithm," *Mol. Phys.* **94**, 727–733 (1998).
- <sup>44</sup>T. J. H. Vlugt, R. Krishna, and B. Smit, "Molecular simulations of adsorption isotherms for linear and branched alkanes and their mixtures in silicalite," *J. Phys. Chem. B* **103**, 1102–1118 (1999).
- <sup>45</sup>T. J. H. Vlugt, "Efficiency of parallel CBMC simulations," *Mol. Simul.* **23**, 63–78 (1999).
- <sup>46</sup>J.-P. Ryckaert and A. Bellemans, "Molecular dynamics of liquid alkanes," *Faraday Discuss. Chem. Soc.* **66**, 95–106 (1978).
- <sup>47</sup>M. G. Martin and J. I. Siepmann, "Transferable potentials for phase equilibria. 1. United-atom description of *n*-alkanes," *J. Phys. Chem. B* **102**, 2569–2577 (1998).
- <sup>48</sup>D. Dubbeldam, A. Torres-Knoop, and K. S. Walton, "On the inner workings of Monte Carlo codes," *Mol. Simul.* **39**, 1253–1292 (2013).
- <sup>49</sup>J. Lennard and I. Jones, "On the determination of molecular fields.—I. From the variation of the viscosity of a gas with temperature," *Proc. R. Soc. London, Ser. A* **106**, 441–462 (1924).
- <sup>50</sup>D. Dubbeldam, S. Calero, T. J. H. Vlugt, R. Krishna, T. L. M. Maesen, and B. Smit, "United atom force field for alkanes in nanoporous materials," *J. Phys. Chem. B* **108**, 12301–12313 (2004).
- <sup>51</sup>P. Bai, M. Tsapatsis, and J. I. Siepmann, "TraPPE-zeo: Transferable potentials for phase equilibria force field for all-silica zeolites," *J. Phys. Chem. C* **117**, 24375–24387 (2013).
- <sup>52</sup>T. J. H. Vlugt and M. Schenk, "Influence of framework flexibility on the adsorption properties of hydrocarbons in the zeolite silicalite," *J. Phys. Chem. B* **106**, 12757–12763 (2002).
- <sup>53</sup>H. A. Lorentz, "Ueber die anwendung des satzes vom virial in der kinetischen theorie der gase," *Ann. Phys.* **248**, 127–136 (1881).
- <sup>54</sup>D. Berthelot, "Sur le mélange des gaz," *C. R.* **126**, 15 (1898).
- <sup>55</sup>C. Baerlocher, L. B. McCusker, and D. H. Olson, *Atlas of Zeolite Framework Types*, 6th ed. (Elsevier, Amsterdam, 2007).
- <sup>56</sup>D.-Y. Peng and D. B. Robinson, "A new two-constant equation of state," *Ind. Eng. Chem. Fundam.* **15**, 59–64 (1976).
- <sup>57</sup>D. Dubbeldam, S. Calero, D. E. Ellis, and R. Q. Snurr, "RASPA: Molecular simulation software for adsorption and diffusion in flexible nanoporous materials," *Mol. Simul.* **42**, 81–101 (2016).
- <sup>58</sup>D. Nicholson and N. G. Parsonage, *Computer Simulation and the Statistical Mechanics of Adsorption* (Academic Press, New York, 1988).
- <sup>59</sup>B. Smit, "Grand canonical Monte Carlo simulations of chain molecules: Adsorption isotherms of alkanes in zeolites," *Mol. Phys.* **85**, 153–172 (1995).
- <sup>60</sup>T. O. Bok, E. P. Andriako, E. E. Knyazeva, and I. I. Ivanova, "Engineering of zeolite BEA crystal size and morphology via seed-directed steam assisted conversion," *RSC Adv.* **10**, 38505–38514 (2020).
- <sup>61</sup>T. J. H. Vlugt, W. Zhu, F. Kapteijn, J. A. Moulijn, B. Smit, and R. Krishna, "Adsorption of linear and branched alkanes in the zeolite silicalite-1," *J. Am. Chem. Soc.* **120**, 5599–5600 (1998).
- <sup>62</sup>R. Krishna, B. Smit, and S. Calero, "Entropy effects during sorption of alkanes in zeolites," *Chem. Soc. Rev.* **31**, 185–194 (2002).
- <sup>63</sup>Z. Du, G. Manos, T. J. H. Vlugt, and B. Smit, "Molecular simulation of adsorption of short linear alkanes and their mixtures in silicalite," *AIChE J.* **44**, 1756–1764 (1998).
- <sup>64</sup>R. Krishna and J. M. van Baten, "Entropy-based separation of linear chain molecules by exploiting differences in the saturation capacities in cage-type zeolites," *Sep. Purif. Technol.* **76**, 325–330 (2011).